Competing polar and antipolar phases in $n = 2$ Ruddlesden-Popper niobates and tantalates from first principles

Kishwar-E Hasin and Elizabeth A. Nowadnick*
Department of Materials Science and Engineering, University of California, Merced, California 95343, USA

(Received 7 September 2023; accepted 9 November 2023; published 7 December 2023)

The Li-based layered perovskites $Li_2AB_2O_7$ (A = Ca, Sr; B = Nb, Ta) host competing ferroelectric and antiferroelectric states which arise from coupled octahedral rotation distortions and (anti)polar instabilities. We combine density functional theory (DFT) calculations with group theoretic analysis to unravel the mechanism that controls the relative energies of these competing states. We identify transition paths between the competing polar and antipolar states with very low-energy barriers (<3 meV/f.u.), and show that stacking domain walls can facilitate an antipolar-polar transition. We furthermore show that epitaxial strain tunes the relative energy between the polar and antipolar phases. We compare the $Li_2AB_2O_7$ materials to other families of layered perovskite oxide (anti)ferroelectrics.

DOI: 10.1103/PhysRevMaterials.7.124402

I. INTRODUCTION

Ferroelectrics and antiferroelectrics are both classes of materials that are of great fundamental and applied interest due to their structural phase transitions, complex domain structures, and applications in low-power electronics and energy storage devices [1–3]. Ferroelectrics have polar crystal structures with a polarization that can be reversed in direction by an applied electric field, whereas antiferroelectrics have a nonpolar ground state and a low-energy polar phase which can be reached via an electric-field-driven first-order phase transition. Both ferroelectricity and antiferroelectricity have been intensively investigated in the context of ABO_3 perovskites, with prototypical examples being ferroelectric $BaTiO_3$ and antiferroelectric $PbZrO_3$. Ferroelectricity in oxide perovskites typically arises from the second-order Jahn-Teller effect or from lone pair-active cations [4,5], whereas antiferroelectricity generally arises from a complex competition of structural phases. [6,7].

In the past decade, significant interest has developed in ferroelectricity in layered perovskites, which are materials where perovskite slabs interleave with other structural units. The discovery of hybrid improper ferroelectricity in $n = 2$ Ruddlesden-Popper (RP) oxides (chemical formula $A_3B_2O_7$), whereby polarization is induced via a trilinear coupling to octahedral rotation distortions [8,9], has led to the discovery of several room-temperature ferroelectrics [10–14]. In addition, further studies have revealed that these materials exhibit very flat energy landscapes with multiple competing structural phases that are close in energy [15–17]. This facilitates low ferroelectric switching barriers and other properties such as complex domain structures [18] and nanoscale polar/nonpolar phase coexistence [19]. Interestingly, competing low-energy nonpolar phases also exhibit trilinear couplings between octahedral rotations and antipolar distortions, which has motivated proposals that antiferroelectricity could arise via a mechanism analogous to hybrid improper ferroelectricity in $n = 2$ RPs [11].

A closely related family of layered perovskites are the $Li_2AB_2O_7$ (A = Ca, Sr; B = Nb, Ta) materials [20]. The crystal structure of $Li_2AB_2O_7$ consists of slabs containing two ABO_3 perovskite layers alternating with Li_2O layers (instead of AO rocksalt layers as in the $A_3B_2O_7$ RPs). These Li-based RPs have been been studied for their possible applications in Li-ion conduction [21] and CO_2 capture [22]. In the past few years, the $Li_2AB_2O_7$ materials have emerged as a family of (anti)ferroelectric materials. Experiments have revealed a rich structural phase diagram, with different studies reporting several competing polar and nonpolar phases as well as both ferroelectricity and antiferroelectricity [23–29]. In addition, density functional theory (DFT) calculations have reported that these competing polar and nonpolar phases are extremely close in energy (<1 meV/f.u. for $Li_2SrNb_2O_7$) [23]. This indicates a much flatter energy landscape than the $A_3B_2O_7$ RPs, where the energy difference between the polar ground state and lowest-energy nonpolar phase is typically >10 meV/f.u. [14,17]. However, open questions remain about the mechanism that controls the relative energies of the competing polar/nonpolar phases of $Li_2AB_2O_7$, as well as the transition pathway between these phases which is critical for (anti)ferroelectricity. In this paper, we combine DFT calculations with group theoretic analysis to take steps toward addressing these questions.

Figure 1(a) shows the crystal structure of the $Li_2AB_2O_7$ materials in the high-symmetry $I4/mmm$ reference phase. The adjacent perovskite slabs are offset from each other by a distance of $(a_0/2)[110]$, and the Li cations are situated directly above/below the perovskite equatorial oxygen atoms. The crystal structures of the various competing phases in $Li_2AB_2O_7$ are distorted by sets of atomic displacements that lower the symmetry from $I4/mmm$. At room temperature,

*enowadnick@ucmerced.edu

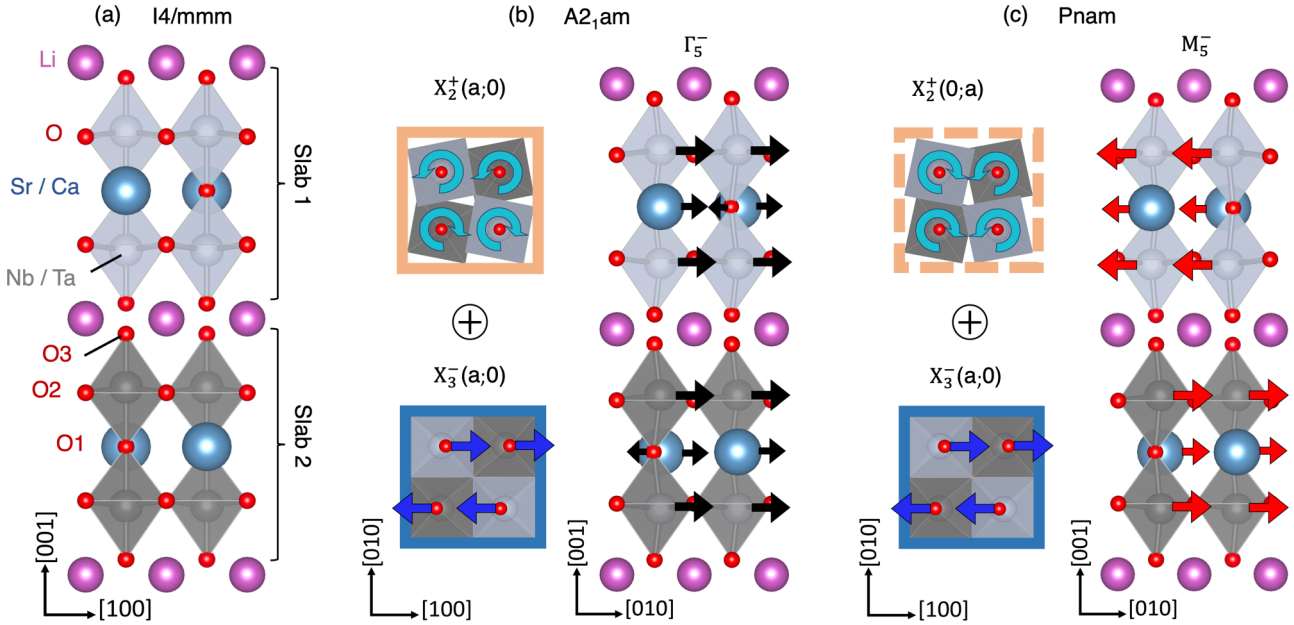

FIG. 1. Crystal structure of $Li_2AB_2O_7$ (A = Ca, Sr; B = Nb, Ta): (a) High-symmetry $I4/mmm$ reference structure, (b) polar $A2_1am$ structure, and (c) antipolar $Pnam$ structure. The upper and lower perovskite slabs are colored light and dark gray, respectively. The $A2_1am$ ($Pnam$) structure can be decomposed with respect to $I4/mmm$ into three structural distortions [(b) and (c)]: an out-of-phase octahedral rotation that transforms like X_3^- (highlighted in blue boxes), an in-phase octahedral rotation that transforms like X_2^+ (orange boxes), and a polar (antipolar) distortion that transforms like Γ_5^- (M_5^-). The X_3^- octahedral rotation is identical in the two structures [lies along the $(a, 0)$ order parameter direction], whereas the X_2^+ octahedral rotation is along the $(a, 0)$ direction in $A2_1am$ and along the $(0, a)$ direction in $Pnam$. As a result, the sense of the X_2^+ octahedral rotation in $A2_1am$ and $Pnam$ is the same in perovskite slab 2 (dark gray) and the opposite in slab 1 (light gray). For clarity, the X_3^- and X_2^+ distortions in (b) and (c) are viewed along the [001] axis, and the Li and Ca/Sr atoms are suppressed. Distortion amplitudes in this figure are artificially increased for better visualization, and the atomic displacements are highlighted with arrows.

Uppuluri *et. al.* [23] reported that $Li_2SrNb_2O_7$ crystallizes in the orthorhombic polar $A2_1am$ space group and then transitions to a nonpolar orthorhombic $Pnam$ structure at 200 K. The $A2_1am$ structure can be decomposed into three structural distortions with different symmetries [Fig. 1(b)]: an out-of-phase ($a^-a^-c^0$ in Glazer notation) octahedral rotation that transforms like the irreducible representation (irrep) X_3^-, an in-phase ($a^0a^0c^+$) octahedral rotation that transforms like X_2^+, and a polar distortion that transforms like Γ_5^-. The $Pnam$ structure, shown in Fig. 1(c), is closely related to $A2_1am$ and can be decomposed into the same X_3^- and X_2^+ octahedral rotations (although the sense of the X_2^+ rotation in adjacent perovskite slabs is reversed), together with an antipolar distortion that transforms like M_5^-. We note that the $A_3B_2O_7$ hybrid improper ferroelectrics crystallize in the same $A2_1am$ structure, with the $Pnam$ structure (which is higher in energy in these materials) playing an important role in the ferroelectric switching process [17].

In contrast, several other works have reported that, at room temperature, $Li_2SrNb_2O_7$ crystallizes in the nonpolar $Amam$ phase (X_3^- octahedral rotation only), and then at 217 K, it transitions to a polar $P2_1an$ phase [24,27,28]. The polar $P2_1an$ phase is a subgroup of $Pnam$: in addition to the three distortions shown in Fig. 1(c), there is a polar distortion along the [001] direction which transforms like Γ_3^-. However, DFT calculations have shown that $Li_2SrNb_2O_7$ in the $Pnam$ structure is dynamically stable and have not identified an instability to the $P2_1an$ phase [24,27].

Chemical substitution on the A or B site (Sr $\rightarrow$ Ca or Nb $\rightarrow$ Ta) tunes the structural phase transitions. Substitution of Ta for Nb suppresses the $A2_1am$, $Pnam$, and $Pna2_1$ phases, so that $Li_2SrTa_2O_7$ remains in the $Amam$ phase down to low temperature [29,30]. The suppression of ferroelectricity by Ta substitution is well documented in Nb-based perovskite ferroelectrics such as $KNbO_3$ [31,32]. Substitution of Ca for Sr reduces the perovskite tolerance factor and hence enhances the octahedral rotation amplitudes. Experiments have reported that $Li_2CaTa_2O_7$ has $Pna2_1$ symmetry at room temperature and then transitions to $Pnam$ at 490 K and subsequently to $Amam$ at 930 K [25,26,33]. DFT calculations on $Li_2CaTa_2O_7$ found that the $Pna2_1$ structure is $\sim$0.1 meV/f.u. lower than $Pnam$ [33]. $Li_2Ca_2Nb_2O_7$ has not been reported experimentally to our knowledge, which has been attributed to large octahedral rotations destabilizing the structure [20].

Arising from this plethora of reported $Li_2AB_2O_7$ structural phases, several mechanisms for anti(ferroelectricity) in these materials have been proposed. The presence of a trilinear coupling between octahedral rotations and (anti)polar distortions in the $A2_1am$ and $Pnam$ phases has led to proposals for hybrid improper (anti)ferroelectricity, whereas the lone pair-active Nb^{5+} cation can give rise to proper ferroelectricity (particularly with regard to the $Pnam \rightarrow Pna2_1$ transition). Previous work has argued that both proper and hybrid-improper ferroelectric mechanisms are active at the same time in the $Li_2AB_2O_7$ materials, with the relative importance of each mechanism being tunable by substituting

TABLE I. Decomposition of the DFT-relaxed and experimental *Pnam* and $A2_1am$ phases of $Li_2SrNb_2O_7$ with respect to the high-symmetry $I4/mmm$ reference structure. Distortion amplitudes are expressed in Å for a 48-atom cell. The experimental structures are obtained from Ref. [23]. $O2_{||}$ and $O2_{\perp}$ refer to O2 displacements parallel and perpendicular to the B-O2 bond, respectively, and $O2_z$ are displacements along [001].

	Mode amplitude (Å)											
	Pnam						$A2_1am$					
	X_2^+		X_3^-		M_5^-		X_2^+		X_3^-		Γ_5^-	
Atoms	DFT	Expt.	DFT	Expt.	DFT	Expt.	DFT	Expt.	DFT	Expt.	DFT	Expt.
Li	−0.01	0.41	0.60	0.62	0.07	−0.35	0.07	−0.06	0.60	0.50	0.04	0.35
Sr	–	–	−0.06	−0.02	0.19	−0.13	–	–	−0.06	−0.05	−0.13	−0.01
Nb	–	–	−0.06	−0.01	−0.27	−0.05	–	–	−0.06	−0.02	−0.17	−0.22
O1	–	–	0.52	0.48	0.03	−0.24	–	–	0.52	0.42	0.09	0.04
$O2_{||}$	0.01	0.01	–	–	0.05	−0.21	−0.01	0.09	–	–	0.03	−0.07
$O2_{\perp}$	−0.20	−0.11	–	–	−0.02	0.17	−0.18	−0.08	–	–	0.05	−0.03
$O2_z$	–	–	0.78	0.69	–	–	–	–	0.78	0.74	–	–
O3	–	–	−0.51	−0.55	−0.01	0.14	–	–	−0.51	−0.47	0.08	−0.04
Total	0.20	0.43	1.23	1.18	0.35	0.54	0.19	0.14	1.23	1.09	0.26	0.42

Ca → Sr and Nb → Ta [25,27]. Interestingly, a combined proper/hybrid improper ferroelectric mechanism was also recently reported in a layered Dion-Jacobson perovskite [34].

The plan for the rest of this paper is as follows. After summarizing our methods in Sec. II, we analyze the reported low-energy polar and nonpolar structures in Sec. III. We understand how structural instabilities and couplings between structural order parameters control the relative energetics of these phases using bulk calculations on a family of metastable phases in Sec. IV and energy surface calculations in Sec. V. In Sec. VI, we explore energy barriers between the polar and nonpolar phases and discuss their relation to stacking domain walls. In Sec. VII, we investigate the effect of epitaxial strain. Finally, in Sec. VIII, we conclude.

II. METHODS

We perform DFT calculations using VASP [35,36] with the PBEsol functional [37,38]. The projector-augmented-wave pseudopotentials used for the calculation are Li_sv ($1s^2 2s^1$), Ca_sv ($3s^2 3p^6 4s^2$), Sr_sv ($4s^2 4p^6 5s^2$), Nb_sv ($4s^2 4p^6 5s^2 4d^3$), Ta ($6s^2 5d^3$), and O ($2s^2 2p^4$). We use a 48-atom computational unit cell with a $6 \times 6 \times 2$ Monkhorst-Pack k-point mesh and a plane-wave cutoff of 600 eV. We employ a force convergence tolerance of 2.0 meV/Å for structural relaxations. To calculate transition paths between the competing phases, we use the nudged elastic band (NEB) method [39] to relax the intermediate structures. The ionic positions, lattice parameters, and volume of the intermediate structures are allowed to relax in the NEB calculations with an increased force convergence tolerance of 10 meV/Å. The ISODISTORT, ISOTROPY, ISOVIZ, ISOCIF, and FINDSYM tools from the ISOTROPY software suite [40] are used for group theoretic analysis, and VESTA [41] is used for crystal structure visualization.

III. LOW-ENERGY POLAR AND ANTIPOLAR STRUCTURES

We start our investigation by using DFT to perform structural relaxations of the $Li_2AB_2O_7$ (A = Ca, Sr; B = Nb, Ta) materials with symmetry constrained to space groups *Pnam* and $A2_1am$. In agreement with previous DFT calculations [23,27,33], we find that *Pnam* is slightly lower in energy than $A2_1am$. We decompose these structures with respect to the high-symmetry reference structure $I4/mmm$ to obtain struc-

TABLE II. Total energy of $Li_2AB_2O_7$ (A = Sr, Ca; B = Nb, Ta) in various structural phases calculated from DFT structural relaxations. Energies are reported in meV/f.u. with respect to the energy of $I4/mmm$. Order parameter directions that establish each space group are given.

		Energy (meV/f.u.)			
Space group	Irrep	$Li_2SrNb_2O_7$	$Li_2SrTa_2O_7$	$Li_2CaNb_2O_7$	$Li_2CaTa_2O_7$
$F2mm$	$\Gamma_5^-(a, a)$	−1.73	0.00	−44.91	−6.55
$Amam$	$M_5^-(0, a)$	−2.45	−0.03	−47.57	−6.85
$Acam$	$X_2^+(a; 0)$	−0.03	−0.03	−136.19	−79.21
$Amam$	$X_3^-(a; 0)$	−53.93	−40.95	−321.61	−301.42
$P4_2/mnm$	$X_3^-(a; a)$	−41.55	−33.14	−275.61	−261.80
$A2_1am$	$X_2^+(a; 0) \oplus X_3^-(a; 0) \oplus \Gamma_5^-(a, a)$	−57.25	−40.88	−422.39	−367.09
Pnam	$X_2^+(0; a) \oplus X_3^-(a; 0) \oplus M_5^-(0, a)$	−57.90	−40.93	−427.42	−373.11

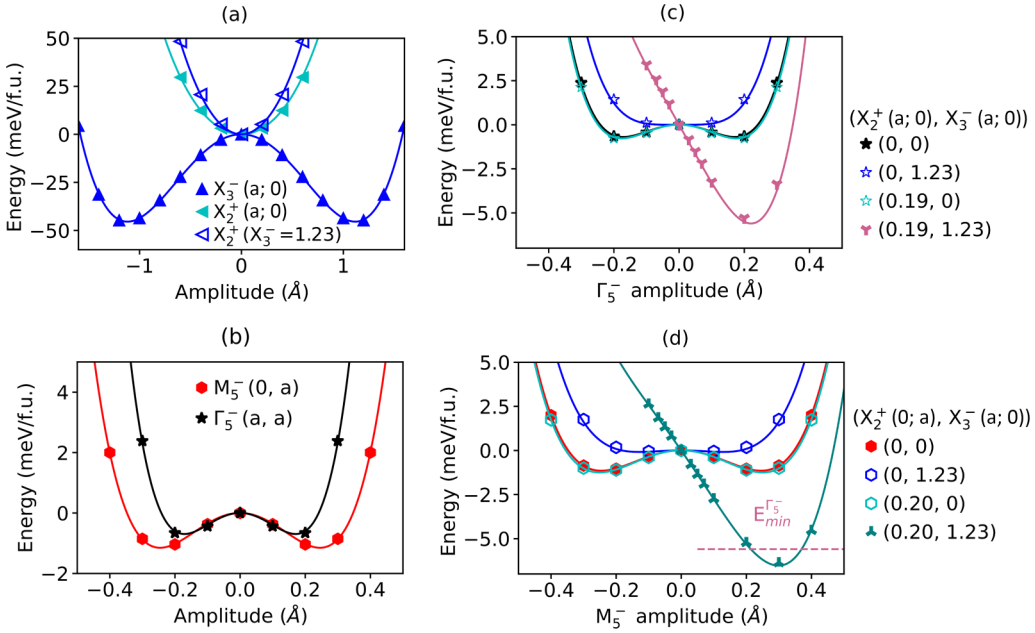

FIG. 2. $Li_2SrNb_2O_7$ energy surfaces: Energy as a function of distortion amplitude for (a) the X_3^- and X_2^+ octahedral rotations, and (b) and (c) the polar Γ_5^- and (b) and (d) antipolar M_5^- distortions. The solid markers indicate energy surfaces where a single distortion is frozen into $I4/mmm$, which are used to extract the α_i and β_i coefficients in Table III. The open markers indicate energy surfaces used to extract the biquadratic δ_i coefficients, where a fixed amplitude of one distortion (given in the legend in Å for a 48-atom cell) is frozen in, and then a second distortion is frozen in with increasing amplitude. The trilinear coupling coefficients γ_i are extracted by fitting the linear region of the pink and turquoise curves in (c) and (d). For comparison, the curves from (b) are reproduced in (c) and (d). The pink dashed line in (d) shows the energy minimum from (c).

tural distortion amplitudes. The decomposition of both the DFT-relaxed and experimentally reported [23] structures for $Li_2SrNb_2O_7$ are presented in Table I (decompositions for the other three compounds are given in Appendix A). The X_3^- octahedral rotation is the largest amplitude distortion in both the DFT and experimental structures. The majority of the X_3^- amplitude comes from oxygen displacements, although there is a significant Li displacement as well. The X_2^+ octahedral rotation amplitude is much smaller. Finally, the polar (Γ_5^-) and antipolar (M_5^-) distortions arise from displacement of the Sr and Nb cations against the oxygen sublattice. These cation displacements are in the same direction in adjacent perovskite slabs in the Γ_5^- polar distortion (yielding a net polarization), whereas they are in opposite directions in the M_5^- antipolar distortion [see Figs. 1(b) and 1(c)]. The M_5^- amplitude in $Pnam$ is larger than the Γ_5^- amplitude in $A2_1am$ (0.35 vs 0.26 Å for the DFT structures). Interestingly, the M_5^- and Γ_5^- distortions contain fairly large Li displacements in the experimental structure which are not present in the DFT-relaxed structures. This difference could arise from factors such as temperature-dependent changes in displacement amplitudes or differences between the experimental and DFT lattice parameters.

Finally, we explore the polar $Pna2_1$ structure which has been reported in several experiments [24–28,33]. This structure is derived from $Pnam$ by adding in a polar distortion along the c axis (which transforms like the Γ_3^- irrep of $I4/mmm$). We freeze a Γ_3^- distortion into the $Pnam$ structure to establish $Pna2_1$ symmetry and then relax this structure with DFT to assess whether it is lower energy than $Pnam$. We find that $Pna2_1$ is 0.1 meV/f.u. lower in energy than $Pnam$ for $Li_2CaNb_2O_7$. In contrast, we find that $Pna2_1$ relaxes back to the $Pnam$ structure for $Li_2SrNb_2O_7$, $Li_2CaTa_2O_7$, and $Li_2SrTa_2O_7$. As a result, we do not consider the $Pna2_1$ structure further in this paper.

IV. METASTABLE STRUCTURAL PHASES

To get further insight into the competing $Pnam$ and $A2_1am$ phases, we next use DFT to perform structural relaxations of our $Li_2AB_2O_7$ materials in various metastable phases. This allows us to probe the (in)stability of different structural distortions and assess how they combine together to create the low-energy phases.

To set the stage, we briefly review the key features of the symmetry framework needed for enumerating and analyzing these distorted structural phases. The distortions introduced above that transform like the X_3^-, X_2^+, Γ_5^-, and M_5^- irreps are each described by a two-dimensional order parameter. These order parameters have three distinct directions: $(a;0)$, $(a;a)$, and $(a;b)$, where a and b are real numbers. Each of these directions defines a different subgroup of $I4/mmm$. For example, the $(a;0)$ direction of X_3^- establishes $Amam$, whereas the $(a;a)$ and $(a;b)$ directions establish $P4_2/mnm$ and $Pnnm$, respectively. To establish the symmetry of the $Pnam$ and $A2_1am$ structures, two out of the three structural order parameters must be specified; then the other is allowed by symmetry. For example, the $A2_1am$ symmetry is established by imposing the $(a;0)$ direction of both the X_3^- and X_2^+ distortions, whereas the

TABLE III. Landau coefficients obtained by fitting the energy surfaces for $Li_2SrNb_2O_7$ in Fig. 2 to the Landau expansions given in Eqs. (1) and (2).

	Subindices					
Coefficients (units)	1	2	3	4	5	6
α (meV/Å^{2}f.u.)	−72.65	74.08	−38.22	−47.69	–	–
β (meV/Å^{4}f.u.)	29.02	25.56	317.20	817.00	–	–
γ (meV/Å^{3}f.u.)	−108.43	−134.69	–	–	–	–
δ (meV/Å^{4}f.u.)	33.56	18.28	−41.46	33.56	30.23	−68.60

Pnam symmetry is established by imposing the $(a; 0)$ direction of X_3^- and the $(0; a)$ direction of X_2^+. Specifying these two distortions is sufficient to establish the $A2_1am$ (*Pnam*) space group; the Γ_5^- (M_5^-) distortion is then allowed by symmetry.

We perform DFT structural relaxations of $Li_2AB_2O_7$ (A = Sr, Ca; B = Nb, Ta) with symmetry constrained to space groups that are established by the X_3^-, X_2^+, Γ_5^-, and M_5^- irreps. We consider space groups established by one of these irreps individually as well as those established by pairs of irreps. The total energies from these calculations are shown in Table II (lattice parameters and distortion amplitudes are given in Appendix A). For $Li_2SrNb_2O_7$, *Pnam* is slightly lower energy (<1 meV/f.u.) than $A2_1am$, in agreement with Ref. [23]. The *Amam* structure (X_3^- octahedral rotations only) is the next lowest in energy. $Li_2CaNb_2O_7$ and $Li_2CaTa_2O_7$ present the same energy ordering of these phases, although the overall energy scale is larger because the smaller size of the Ca ion causes larger distortion amplitudes. Finally, for $Li_2SrTa_2O_7$, we find that the *Pnam* and $A2_1am$ structures relax to the *Amam* phase, which agrees with the experimental observations of *Amam* down to low temperature.

Next, we focus on the structural phases established by the X_2^+, Γ_5^-, and M_5^- distortions individually. As shown in Table II, these phases have symmetries *Acam*, $F2mm$, and *Amam*, respectively. We emphasize that the *Amam* phase established by M_5^- is distinct from the *Amam* established by X_3^-, and from here on, we refer to it as *Amam*(M_5^-) for clarity. Although these phases are quite high in energy compared with the ground state, they provide insight into the (in)stability of $I4/mmm$ with respect to the X_2^+, Γ_5^-, and M_5^- distortions. This information is in turn useful for understanding how these distortions contribute to the low-energy phases. For $Li_2SrNb_2O_7$, we find that the Γ_5^- and M_5^- distortions lower the energy slightly, with *Amam*(M_5^-) being slightly lower energy than $F2mm$ (2.5 vs 1.7 meV/f.u. below $I4/mmm$, respectively). In contrast, the *Acam* structure relaxes to $I4/mmm$, which shows that the X_2^+ distortion is not itself an instability of $I4/mmm$ (and hence, it must be induced via coupling to other unstable distortions in the *Pnam* and $A2_1am$ structures). As expected, none of these distortions are energy lowering in $Li_2SrTa_2O_7$ since this compound is stable in the *Amam* structure.

The *Acam*, $F2mm$, and *Amam*(M_5^-) structures are all lower energy than $I4/mmm$ for $Li_2CaNb_2O_7$ and $Li_2CaTa_2O_7$. Of the three structural phases, *Acam* is the lowest in energy. This contrasts with $Li_2SrNb_2O_7$, where the X_2^+ distortion is stable, and can be understood by noting that replacement of Sr with Ca reduces the tolerance factor and hence enhances instabilities to octahedral rotations. For both compounds, *Amam*(M_5^-) and $F2mm$ are quite close in energy, with *Amam*(M_5^-) being slightly lower in energy. These phases are ∼45 meV/f.u. below $I4/mmm$ in $Li_2CaNb_2O_7$, whereas they are only ∼7 meV/f.u. below $I4/mmm$ in $Li_2CaTa_2O_7$. This difference can be understood based on the stronger lone-pair instability of Nb^{5+} compared with Ta^{5+}.

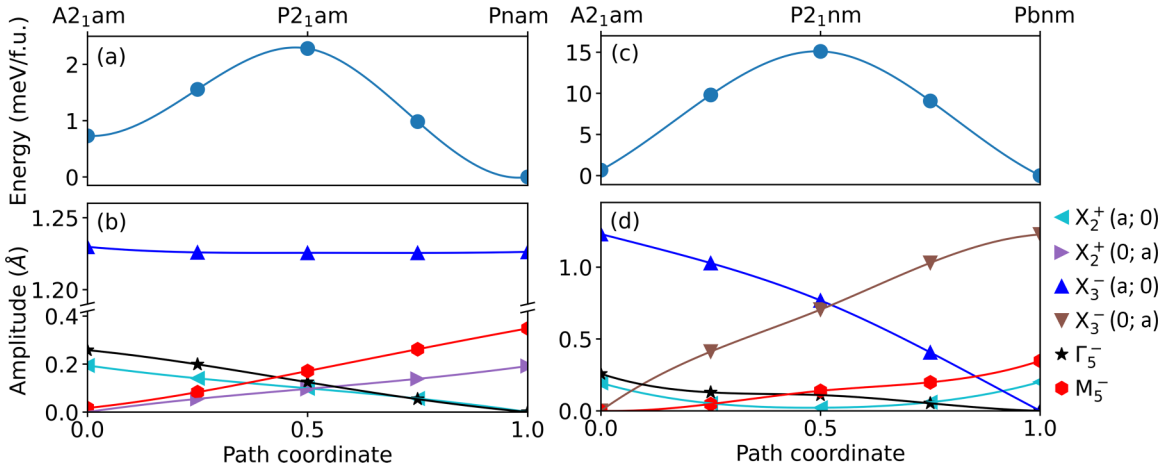

FIG. 3. Energy trajectory for $Li_2SrNb_2O_7$ between polar $A2_1am$ and (a) antipolar *Pnam* and (c) antipolar *Pbnm* (orthorhombic twin of *Pnam*) obtained from nudged elastic band calculations. The intermediate structures have symmetry $P2_1am$ in path (a) and $P2_1nm$ in path (c). (b) and (d) show the evolution of the X_2^+, X_3^-, Γ_5^-, and M_5^- structural distortion amplitudes.

V. LANDAU EXPANSION AND ENERGY SURFACES

The total energies of the metastable phases discussed in the previous section inform us about the instability of $I4/mmm$ to the various distortions; however, they do not tell us about how coupling between these distortions establishes the low-energy $Pnam$ and $A2_1am$ phases. To understand these couplings, it is useful to perform Landau expansions about $I4/mmm$ in terms of the structural distortion amplitudes Q that contribute to the $Pnam$ and $A2_1am$ structures. These expansions, for the $Pnam$ and $A2_1am$ structures, respectively, go as

$$E_{Pnam}(X_3^-, X_2^+, M_5^-) = E(X_3^-) + E(X_2^+) + E(M_5^-) + E_{\text{tri},Pnam} + E_{c,Pnam} \quad (1)$$

and

$$E_{A2_1am}(X_3^-, X_2^+, \Gamma_5^-) = E(X_3^-) + E(X_2^+) + E(\Gamma_5^-) + E_{\text{tri},A2_1am} + E_{c,A2_1am}. \quad (2)$$

Here the single-distortion terms are

$$E(X_3^-) = \alpha_1 Q_{X_3^-}^2 + \beta_1 Q_{X_3^-}^4,$$
$$E(X_2^+) = \alpha_2 Q_{X_2^+}^2 + \beta_2 Q_{X_2^+}^4,$$
$$E(M_5^-) = \alpha_3 Q_{M_5^-}^2 + \beta_3 Q_{M_5^-}^4,$$
$$E(\Gamma_5^-) = \alpha_4 Q_{\Gamma_5^-}^2 + \beta_4 Q_{\Gamma_5^-}^4.$$

There are trilinear coupling terms between the X_3^- and X_2^+ octahedral rotations and the M_5^- (Γ_5^-) distortions:

$$E_{\text{tri},Pnam} = \gamma_1 Q_{X_3^-} Q_{X_2^+} Q_{M_5^-}, \quad (3)$$

$$E_{\text{tri},A2_1am} = \gamma_2 Q_{X_3^-} Q_{X_2^+} Q_{\Gamma_5^-}, \quad (4)$$

and finally, there are biquadratic coupling terms between each pair of structural distortion order parameters:

$$E_{c,Pnam} = \delta_1 Q_{X_3^-}^2 Q_{X_2^+}^2 + \delta_2 Q_{X_3^-}^2 Q_{M_5^-}^2 + \delta_3 Q_{X_2^+}^2 Q_{M_5^-}^2,$$
$$E_{c,A2_1am} = \delta_4 Q_{X_3^-}^2 Q_{X_2^+}^2 + \delta_5 Q_{X_3^-}^2 Q_{\Gamma_5^-}^2 + \delta_6 Q_{X_2^+}^2 Q_{\Gamma_5^-}^2.$$

We obtain the coefficients of these Landau expansions for $Li_2SrNb_2O_7$ by fitting the DFT-computed energy surfaces shown in Fig. 2 and report the results in Table III (energy surfaces and Landau coefficients for $Li_2CaNb_2O_7$, $Li_2CaTa_2O_7$, and $Li_2SrTa_2O_7$ are given in Appendix B).

Figures 2(a) and 2(b) show energy surfaces for $Li_2SrNb_2O_7$ obtained by freezing in each of the X_3^-, X_2^+, Γ_5^-, and M_5^- distortions into the $I4/mmm$ structure individually. As expected, based on the total energy calculations presented in Sec. IV, the X_3^-, Γ_5^-, and M_5^- distortions yield double-well energy surfaces, whereas the X_2^+ energy surface is parabolic, indicating that this distortion is energetically stable. The minimum of the M_5^- energy surface is slightly lower than the minimum of the Γ_5^- surface, again consistent with the bulk energy calculation result that $Amam(M_5^-)$ is slightly lower energy than $F2mm$. Fitting these energy surfaces yields the α_i and β_i coefficients given in Table III. The energy surface in Fig. 2(a) with open symbols is obtained by freezing in a fixed amplitude of the X_3^- distortion (1.23 Å, as indicated in the figure) and then freezing in the X_2^+ distortion on top of that. Fitting this curve yields the biquadratic coupling coefficient δ_1 between the X_3^- and X_2^+ distortions.

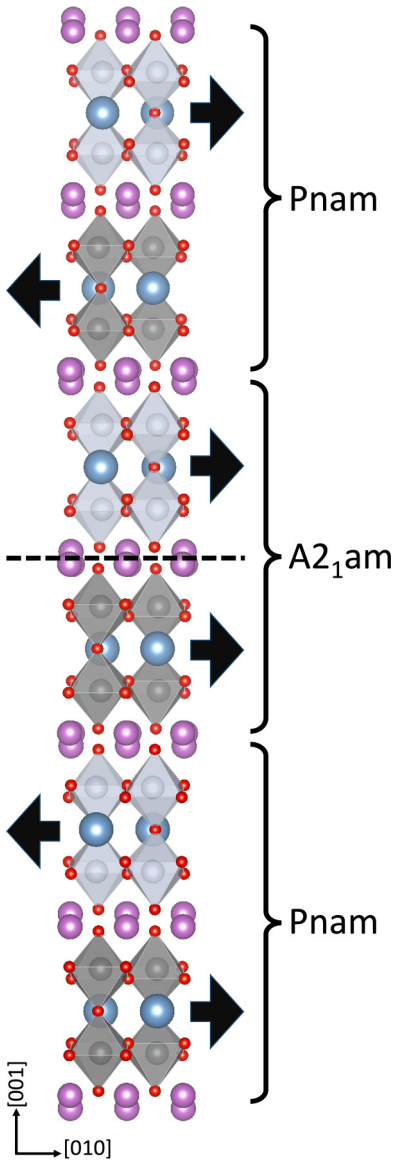

FIG. 4. Schematic of a stacking domain wall (dashed line) in $Li_2SrNb_2O_7$ that can form between antipolar $Pnam$ domains with opposite M_5^- order parameter directions. The local crystal structure at the stacking domain wall is polar $A2_1am$. The black arrows indicate the cation displacement direction in each perovskite slab.

Figures 2(c) and 2(d) explore the couplings between the Γ_5^- (M_5^-) distortions and the octahedral rotations. Fitting the curves with open symbols in Figs. 2(c) and 2(d) gives the biquadratic coupling coefficients. We find an unusual negative biquadratic coupling between the X_2^+ rotation and the M_5^- and Γ_5^- distortions (δ_3 and δ_6 in Table III). To obtain the trilinear coupling coefficients in Eqs. (3) and (4), we impose fixed amplitudes of both the X_3^- and X_2^+ distortions and subsequently freeze in increasing amplitudes of the M_5^- (Γ_5^-) distortions. Both γ_1 and γ_2 are large and negative, indicating the importance of the trilinear term in lowering the total energy of the $Pnam$ and $A2_1am$ structures. These trilinear coupling terms

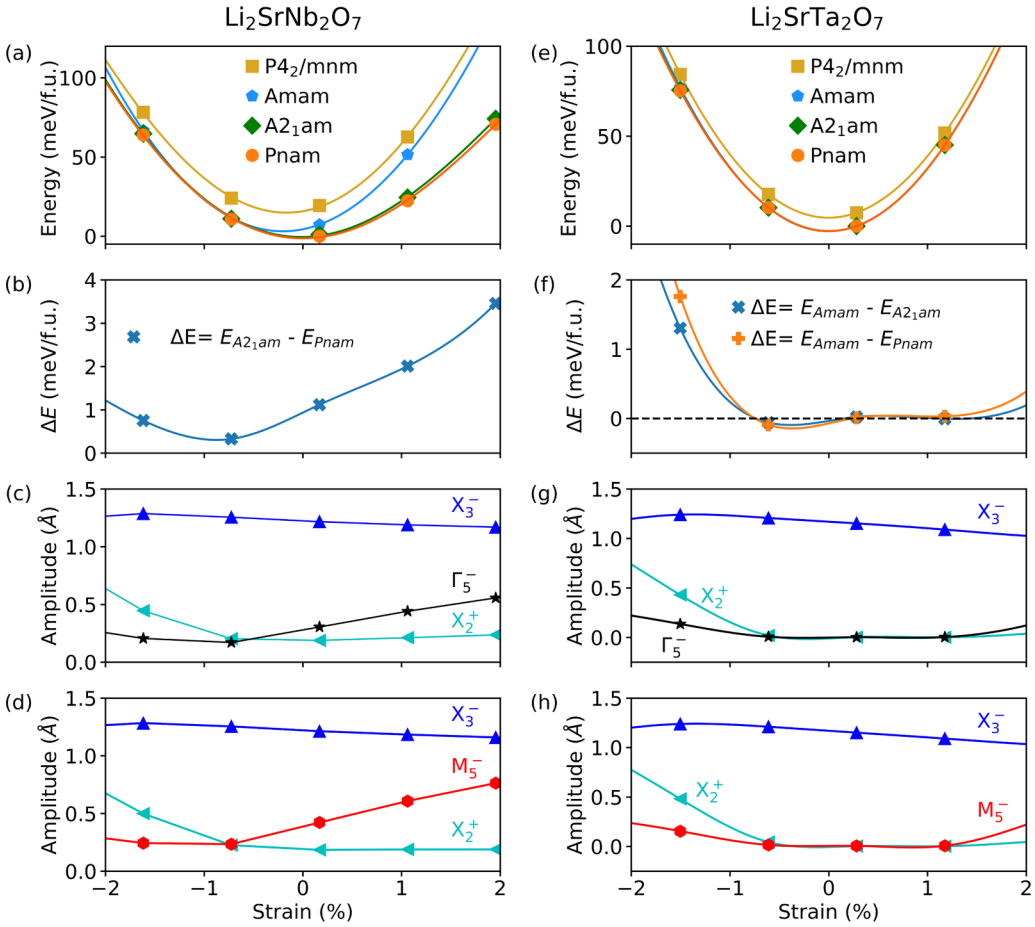

FIG. 5. Impact of epitaxial strain on (a)–(d) $Li_2SrNb_2O_7$ and (e)–(h) $Li_2SrTa_2O_7$. (a) Total energy, (b) energy difference between *Pnam* and $A2_1am$, (c) $A2_1am$ distortion amplitudes, and (d) *Pnam* distortion amplitudes for $Li_2SrNb_2O_7$ as a function of strain. (e) Total energy, (f) energy difference between *Amam* and $A2_1am$ (blue) and *Amam* and *Pnam* (orange), (g) $A2_1am$ distortion amplitudes, and (h) *Pnam* distortion amplitudes for $Li_2SrTa_2O_7$ as a function of strain. The distortion amplitudes are reported for a 48-atom computational cell.

are responsible for inducing the X_2^+ distortion in $Li_2SrNb_2O_7$, which on its own is energetically stable [Fig. 2(a)]. The trilinear coupling does not induce M_5^- (Γ_5^-), which can be seen by noting that the distortion amplitude at which the energy reaches its minimum does not increase when the trilinear coupling is included [compare black and pink (red and turquoise) curves in Figs. 2(c) and 2(d), respectively]. Thus, we find that the slightly lower energy of *Pnam* compared with $A2_1am$ in $Li_2SrNb_2O_7$ can be traced back to the fact that the M_5^- distortion is slightly more energy lowering than the Γ_5^- distortion [Fig. 2(b)]. We note that this contrasts with the $A_3B_2O_7$ hybrid improper ferroelectrics, where unstable X_3^- and X_2^+ distortions induce the polar distortion (which generally is stable on its own) [8]. Instead, $Li_2SrNb_2O_7$ is more similar to the Aurivillius-phase ferroelectrics $SrBi_2(Nb,Ta)_2O_9$, where a hard X_2^+ distortion induced by a trilinear coupling stabilizes the polar ground-state phase [42,43].

Finally, we compare $Li_2SrNb_2O_7$ with $Li_2CaNb_2O_7$ and $Li_2CaTa_2O_7$ (see Appendix B for full details and energy surface plots). In both $Li_2CaNb_2O_7$ and $Li_2CaTa_2O_7$, freezing in the X_2^+, X_3^-, M_5^-, and Γ_5^- distortions yields double-well energy surfaces. The X_2^+ energy surfaces have a lower minimum energy than the M_5^- and Γ_5^- surfaces due to the smaller tolerance factor in these materials. Thus, the role of the trilinear coupling terms in Eqs. (3) and (4) are different in $Li_2SrNb_2O_7$ and the Ca-based materials: In $Li_2SrNb_2O_7$, the trilinear coupling induces the stable X_2^+ distortion, whereas in the Ca-based materials, the trilinear coupling induces a larger value of the M_5^- and Γ_5^- distortions than would be present just from their instabilities alone.

VI. ENERGY BARRIERS BETWEEN POLAR AND ANTIPOLAR PHASES

Having understood the origin of the small energy difference between the *Pnam* and $A2_1am$ phases in the previous sections, we next investigate the energy barrier between these two phases in $Li_2SrNb_2O_7$ using NEB calculations. Figure 3(a) shows the energy trajectory between *Pnam* and $A2_1am$, from which we identify a very low energy barrier between these phases of 2.30 meV/f.u.. The intermediate structures along the trajectory have symmetry $P2_1am$. Figure 3(b) shows the evolution of the distortion amplitudes along this trajectory. Transitioning from $A2_1am$ to *Pnam* involves reversing the sense of the X_2^+ octahedral rotation in every other perovskite slab, which in order parameter language

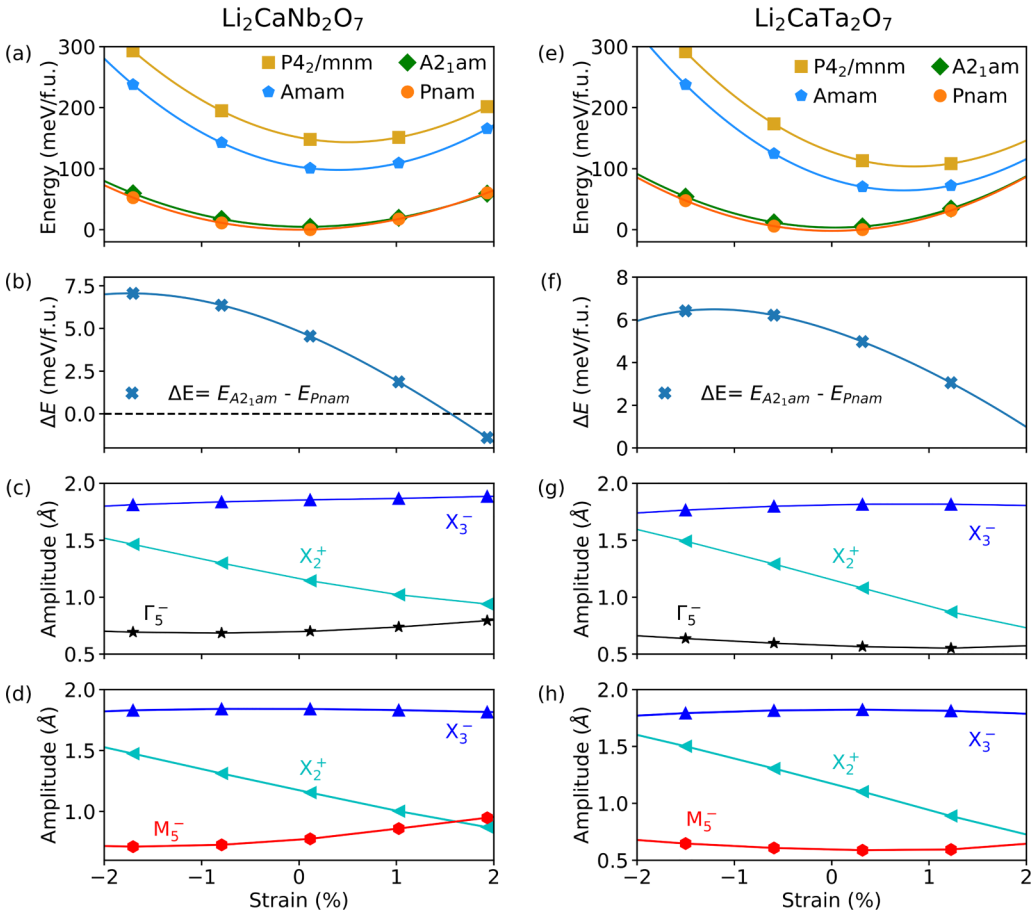

FIG. 6. Impact of epitaxial strain on (a)–(d) $Li_2CaNb_2O_7$ and (e)–(h) $Li_2CaTa_2O_7$: (a) Total energy, (b) energy difference between *Pnam* and $A2_1am$, (c) $A2_1am$ distortion amplitudes, and (d) *Pnam* distortion amplitudes for $Li_2CaNb_2O_7$ as a function of strain. (e) Total energy, (f) energy difference between *Pnam* and $A2_1am$, (g) $A2_1am$ distortion amplitudes, and (h) *Pnam* distortion amplitudes for $Li_2CaTa_2O_7$ as a function of strain. The distortion amplitudes are reported for a 48-atom computational cell.

corresponds to changing the X_2^+ direction from (a; 0) to (0; a), as shown by the cyan and lavender symbols in Fig. 3(b). At the same time, the M_5^- and Γ_5^- distortions turn on and off, respectively [red and black symbols in Fig. 3(b)], whereas the X_3^- distortion is unchanged (blue symbols).

A second possible transition path is to keep the X_2^+ order parameter fixed at (a; 0) and instead change the X_3^- order parameter direction from (a; 0) to (0; a). This corresponds to rotating the axis of the X_3^- octahedral rotations by 90° and establishes an orthorhombic twin of the antipolar structure with symmetry *Pbnm* (distinguished from *Pnam* by a different space group setting). The energy trajectory between $A2_1am$ and *Pbnm* is shown in Fig. 3(c) and gives a higher energy barrier of 15.11 meV/f.u. because it involves changing the larger amplitude X_3^- octahedral rotation. The intermediate structures along the trajectory have $P2_1nm$ symmetry, and the X_3^- amplitude along the (a; 0) direction turns off (blue markers), as the amplitude along the (0; a) direction increases (brown markers) along the transition path [Fig. 3(d)]. The X_2^+ amplitude changes very little, whereas the M_5^- (Γ_5^-) amplitude increases (decreases).

These results suggest that the very low-energy $P2_1am$-barrier path shown in Figs. 3(a) and 3(b) facilitates antiferroelectric behavior in $Li_2SrNb_2O_7$. To understand how this antipolar-polar transition could proceed from a crystal structure perspective, we note that symmetry analysis dictates that the *Pnam* structure has eight structural domains (divided between two orthorhombic twins) [17]. In a bulk multidomain sample with *Pnam* symmetry, we expect that domains with opposite antipolar M_5^- order parameter direction [(0, a) vs (0, $-a$)] can stack along [001], with the interface between them forming a stacking domain wall. Figure 4 shows a schematic of such a domain wall. Locally, at the interface between these antipolar domains, the structure has $A2_1am$ symmetry. Motion of the stacking domain walls along the [001] axis can facilitate a transition an antipolar-polar transition from the *Pnam* to the $A2_1am$ phase. Analogous stacking domain walls have been identified in the polar phase of the $A_3B_2O_7$ hybrid improper ferroelectrics, and their motion facilitates the ferroelectric switching process in these materials [13,17].

VII. EPITAXIAL STRAIN

Finally, we explore the effect of epitaxial strain on the energetics of the low-energy phases of $Li_2AB_2O_7$. We model

TABLE IV. Lattice parameters of DFT-relaxed and experimental structures (in Å) for $Li_2AB_2O_7$ (A = Ca, Sr; B = Nb, Ta).

		$Li_2SrNb_2O_7$		$Li_2SrTa_2O_7$		$Li_2CaNb_2O_7$		$Li_2CaTa_2O_7$	
Space group	Lattice parameter	DFT	Expt.	DFT	Expt.	DFT	Expt.	DFT	Expt.
$I4/mmm$	a	3.947	–	3.949	3.944 [21]	3.919	–	3.925	–
	b	3.947	–	3.949	3.944	3.919	–	3.925	–
	c	17.959	–	18.100	18.176	17.992	–	18.118	–
$F2mm$	a	5.589	–	5.586	–	5.593	–	5.566	–
	b	5.588	–	5.585	–	5.559	–	5.549	–
	c	17.923	–	18.100	–	17.847	–	18.098	–
$Amam$ (M_5^-)	a	5.591	–	5.585	–	5.595	–	5.567	–
	b	5.589	–	5.585	–	5.561	–	5.549	–
	c	17.914	–	18.101	–	17.830	–	18.099	–
$Acam$	a	5.581	–	5.586	–	5.437	–	5.551	–
	b	5.581	–	5.585	–	5.436	–	5.551	–
	c	17.963	–	18.100	–	18.448	–	18.118	–
$Amam$ (X_3^-)	a	5.583	5.59(7) [28]	5.587	5.582 [30]	5.521	–	5.530	5.558 [26]
	b	5.568	5.57(7)	5.575	5.581	5.504	–	5.510	5.551
	c	17.939	17.95(20)	18.044	18.184	17.966	–	18.041	18.504
$P4_2/mnm$	a	5.577	–	5.581	–	5.518	–	5.526	–
	b	5.577	–	5.581	–	5.518	–	5.526	–
	c	17.967	–	18.074	–	18.009	–	18.093	–
$A2_1am$	a	5.589	5.599 [23]	5.587	–	5.536	–	5.515	–
	b	5.578	5.592	5.575	–	5.447	–	5.443	–
	c	17.914	18.010	18.039	–	17.985	–	18.140	–
$Pnam$	a	5.590	5.594 [23]	5.586	–	5.533	–	5.514	5.533 [26]
	b	5.579	5.589	5.574	–	5.442	–	5.439	5.505
	c	17.909	17.933	18.045	–	17.994	–	18.146	18.352

TABLE V. Distortion amplitudes obtained by decomposing the DFT-relaxed structural phases given in Table II with respect to the high-symmetry reference $I4/mmm$. The distortion amplitudes are reported in units of Å for a 48-atom cell.

	Distortion amplitude (Å)															
	$Li_2SrNb_2O_7$				$Li_2SrTa_2O_7$				$Li_2CaNb_2O_7$				$Li_2CaTa_2O_7$			
Space group	Γ_5^-	M_5^-	X_2^+	X_3^-	Γ_5^-	M_5^-	X_2^+	X_3^-	Γ_5^-	M_5^-	X_2^+	X_3^-	Γ_5^-	M_5^-	X_2^+	X_3^-
$F2mm$	0.22	–	–	–	0.00	–	–	–	0.69	–	–	–	0.44	–	–	–
$Amam$ (M_5^-)	–	0.31	–	–	–	0.01	–	–	–	0.79	–	–	–	0.47	–	–
$Acam$	–	–	0.01	–	–	–	0.01	–	–	–	1.66	–	–	–	1.22	–
$Amam$ (X_3^-)	–	–	–	1.23	–	–	–	1.17	–	–	–	1.94	–	–	–	1.94
$P4_2/mnm$	–	–	–	1.04	–	–	–	1.01	–	–	–	1.66	–	–	–	1.66
$A2_1am$	0.26	–	0.19	1.23	0.00	–	0.00	1.17	0.73	–	1.19	1.87	0.60	–	1.18	1.82
$Pnam$	–	0.35	0.20	1.23	–	0.01	0.01	1.18	–	0.80	1.22	1.86	–	0.63	1.21	1.84

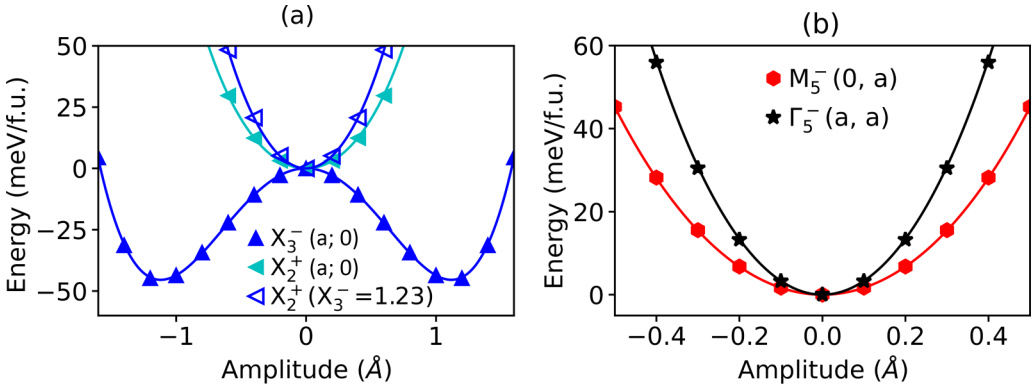

FIG. 7. $Li_2SrTa_2O_7$ energy surfaces: Energy as a function of distortion amplitude for (a) the $X_3^-(a; 0)$ and $X_2^+(a; 0)$ octahedral rotations, and (b) the polar $\Gamma_5^-(a, a)$ and antipolar $M_5^-(0, a)$ distortions.

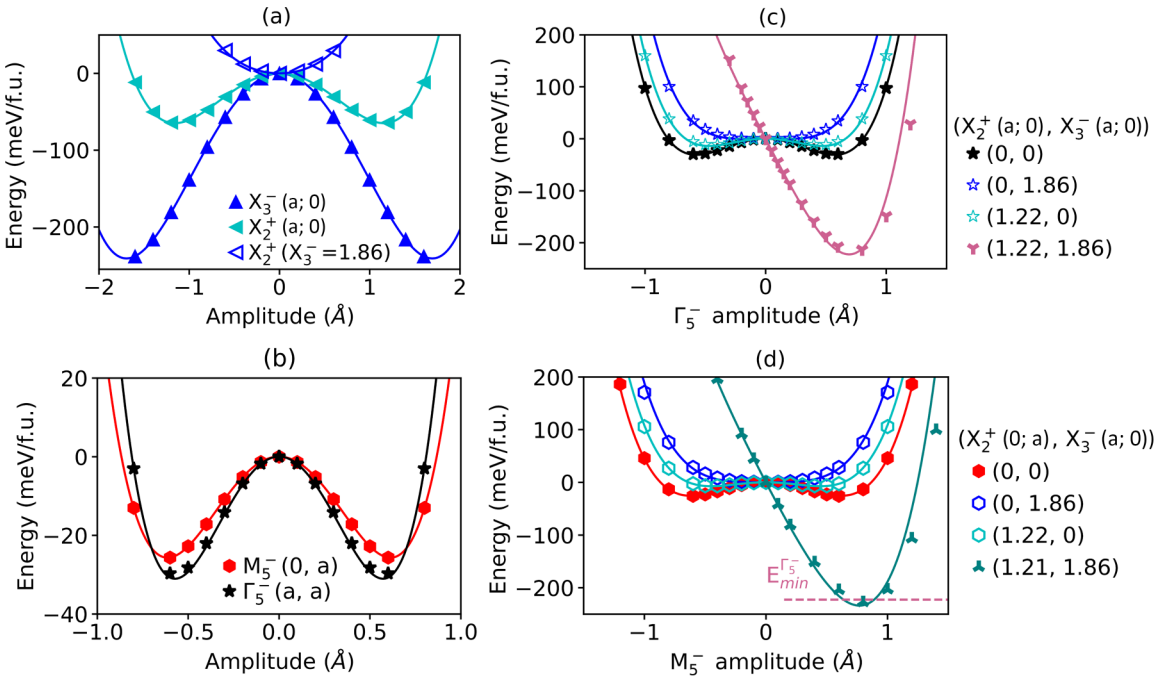

FIG. 8. $Li_2CaNb_2O_7$ energy surfaces: Energy as a function of distortion amplitude for (a) the $X_3^-(a; 0)$ and $X_2^+(a; 0)$ octahedral rotations, and (b) and (c) the polar $\Gamma_5^-(a, a)$ and (b) and (d) antipolar $M_5^-(0, a)$ distortions. The pink (turquoise) curves in (c) and (d) are computed by imposing a fixed amplitude of the X_3^- and X_2^+ distortions, and then computing the energy as a function of polar (antipolar) distortion amplitude. For comparison, the curves from (b) are reproduced in (c) and (d).

strain by performing strained-bulk calculations: We impose a square biaxial constraint in the *ab* plane and allow the *c*-lattice constant and all internal atomic positions to relax. Energy and distortion amplitudes as a function of strain are shown in Fig. 5 for $Li_2Sr(Nb/Ta)_2O_7$ and in Fig. 6 for $Li_2Ca(Nb/Ta)_2O_7$.

Focusing first on $Li_2SrNb_2O_7$, Fig. 5(a) shows that *Pnam* and $A2_1am$ remain very close in energy over the whole strain range that we examine (±2% strain). Figure 5(b) shows the energy difference $\Delta E = E_{A2_1am} - E_{Pnam}$ between the $A2_1am$ and *Pnam* phases. This energy difference is positive at all strain values, indicating that *Pnam* remains the lowest-energy

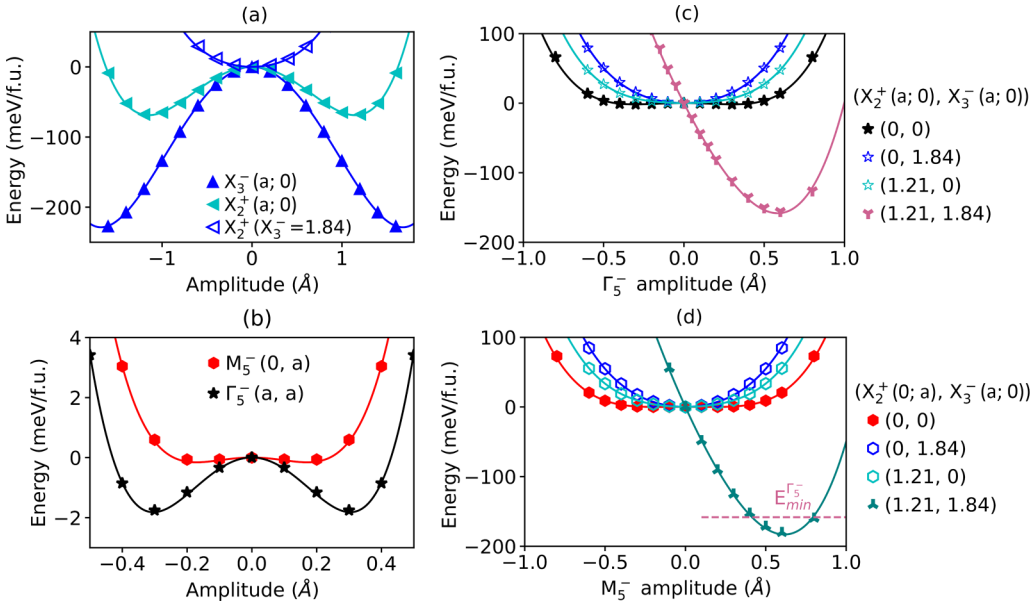

FIG. 9. $Li_2CaTa_2O_7$ energy surfaces: Energy as a function of distortion amplitude for (a) the $X_3^-(a; 0)$ and $X_2^+(a; 0)$ octahedral rotations, and (b) and (c) the polar $\Gamma_5^-(a, a)$ and (b) and (d) antipolar $M_5^-(0, a)$ distortions. The pink (turquoise) curves in (c) and (d) are computed by imposing a fixed amplitude of the X_3^- and X_2^+ distortions, and then computing the energy as a function of polar (antipolar) distortion amplitude. For comparison, the curves from (b) are reproduced in (c) and (d).

TABLE VI. Coefficients obtained by fitting the energy surfaces of $Li_2SrTa_2O_7$ in Fig. 7 to the Landau expansions given in Eqs. (1) and (2).

	Subindices			
Coefficients (units)	1	2	3	4
α (meV/Å^{2}f.u.)	−60.96	140.73	166.53	404.83
β (meV/Å^{4}f.u.)	27.40	15.49	56.74	34.11

phase. The minimum energy difference $\Delta E = 0.31$ meV/f.u. occurs at ∼0.9% compressive strain. Figures 5(c) and 5(d) show the strain evolution of the $A2_1am$ and $Pnam$ distortion amplitudes, respectively. For both structures, the X_3^- octahedral rotation amplitude decreases very slightly, going from compressive to tensile strain. The X_2^+ octahedral rotation also does not change much, except for compressive strains >∼1% when it starts to increase significantly. This accommodates the shrinking lattice parameters in the *ab* plane by increasing the Nb-O-Nb bond angles. At the same (1% compressive) strain, the Γ_5^- and M_5^- amplitudes reach their minimum value. Both these distortion amplitudes grow significantly with increasing tensile strain. The M_5^- amplitude increases more, which explains why ΔE in Fig. 5(b) becomes larger under tensile strain.

Figures 5(e) and 5(h) show the energetics and distortion amplitudes for $Li_2SrTa_2O_7$ as a function of strain. Since $Amam$ is the bulk ground state of $Li_2SrTa_2O_7$, Fig. 5(f) shows the energy differences between this phase and $A2_1am$ (blue) or $Pnam$ (orange). As expected, for small strains, $\Delta E = 0$, indicating that $A2_1am$ and $Pnam$ relax to $Amam$. However, for compressive strains >∼1%, ΔE becomes positive, indicating that these phases are lower in energy than $Amam$ (with $Pnam$ being the lowest-energy phase). This transition to $Pnam$ also is evident from the distortion amplitudes in Figs. 5(g) and 5(h): The X_2^+, M_5^-, and Γ_5^- distortions become nonzero, with the X_2^+ amplitude increasing the most for compressive strains >1%. The X_3^- amplitude decreases very slightly, going from compressive to tensile strain.

The strain evolution of the the Ca-based materials is different from their Sr-based counterparts, although the behaviors of $Li_2CaNb_2O_7$ [Figs. 6(a)–6(d)] and $Li_2CaTa_2O_7$ [Figs. 6(e)–6(h)] are qualitatively similar to each other. For $Li_2CaNb_2O_7$ [Figs. 6(a)–6(d)], $Pnam$ remains the lowest energy under compressive and moderate tensile strains, but then ∼1.5% tensile strain, the $A2_1am$ structure becomes the lowest energy. $Li_2CaTa_2O_7$ shows a similar trend [Figs. 6(e)–6(h)]: The energy difference between $Pnam$ and $A2_1am$ gets smaller, but there is no crossover to $A2_1am$ within the strain values of our calculations. Examining the distortion amplitudes, for both materials, the X_3^- amplitude increases very slightly with strain, whereas the X_2^+ amplitude decreases. In $Li_2CaNb_2O_7$, the Γ_5^- and M_5^- amplitudes increase with strain, whereas in $Li_2CaTa_2O_7$, they decrease slightly.

VIII. DISCUSSION

In this paper, we present a systematic analysis of the competing low-energy structural phases of $Li_2AB_2O_7$ (A = Sr, Ca; B = Nb, Ta). DFT calculations show that the antipolar $Pnam$ structure is slightly lower in energy than the polar $A2_1am$ structure in $Li_2SrNb_2O_7$, $Li_2CaNb_2O_7$, and $Li_2CaTa_2O_7$. We identify a subtle difference between the mechanism for stabilizing these competing phases in $Li_2SrNb_2O_7$ and $Li_2Ca(Nb,Ta)_2O_7$. In $Li_2SrNb_2O_7$, the X_3^- and M_5^- (Γ_5^-) distortions are unstable, and a trilinear coupling induces the stable X_2^+ distortion. The slightly lower energy of $Pnam$ can be traced back to the M_5^- antipolar distortion being slightly more energy lowering than the polar Γ_5^- distortion. In contrast, all the distortions are unstable in the Ca-based materials, with the X_2^+ distortion being significantly more unstable than M_5^- (Γ_5^-). For these materials, the trilinear coupling induces a part of the M_5^- (Γ_5^-) amplitude. Due to these differences, (anti)ferroelectricity in $Li_2SrNb_2O_7$ arises from a proper mechanism, whereas in $Li_2Ca(Nb,Ta)_2O_7$, it arises from a combination of proper and hybrid improper mechanisms. Although in this paper we do not explicitly consider the $Pna2_1$ phase which has been reported in several experiments [24–28,33], we believe that our results are applicable for understanding $Pna2_1$ as well because it is derived from a very small distortion to the $Pnam$ structure.

It is instructive to compare the $Li_2AB_2O_7$ materials with other layered perovskite (anti)ferroelectrics with symmetry-allowed trilinear coupling. The coupled distortions in these Li-based materials have the same symmetries (and hence

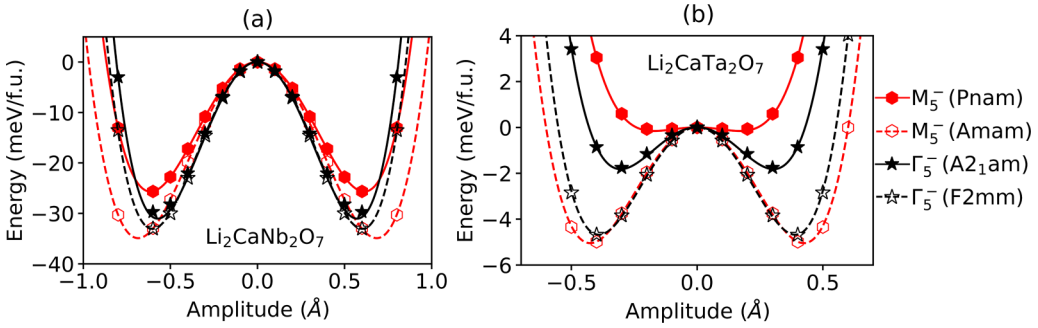

FIG. 10. Energy as a function of $\Gamma_5^-(a, a)$ and $M_5^-(0, a)$ distortion amplitudes for (a) $Li_2CaNb_2O_7$ and (b) $Li_2CaTa_2O_7$. The energy surfaces shown with the solid markers and lines are obtained using atomic displacements from the DFT-relaxed $Pnam$ (red) and $A2_1am$ (black) structures, whereas those shown with the open markers and dashed lines are obtained using atomic displacements from the DFT-relaxed $Amam$ (red) and $F2mm$ (black) structures.

TABLE VII. Coefficients obtained by fitting the energy surfaces of $Li_2CaNb_2O_7$ in Fig. 8 to the Landau expansions given in Eqs. (1) and (2).

	Subindices					
Coefficients (units)	1	2	3	4	5	6
α (meV/Å^{2}f.u.)	−167.84	−96.80	−136.65	−189.46	–	–
β (meV/Å^{4}f.u.)	29.22	36.08	181.70	289.03	–	–
γ (meV/Å^{3}f.u.)	−194.40	−198.25	–	–	–	–
δ (meV/Å^{4}f.u.)	47.52	41.62	42.48	47.52	50.32	41.94

are described by the same irreps X_3^-, X_2^+, Γ_5^-, and M_5^-) as the distortions in the $A_3B_2O_7$ hybrid improper ferroelectrics [8] as well as the $n = 2$ Aurivillius ferroelectrics such as $SrBi_2(Nb,Ta)_2O_9$ [42], although the atomic displacement patterns are somewhat different. Although the antipolar *Pnam* phase is slightly lower in energy than polar $A2_1am$ in the Li-based materials, $A2_1am$ is the ground state of both the $A_3B_2O_7$ and Aurivillius ferroelectrics, with *Pnam* being higher in energy, ∼10 meV/f.u. in the $A_3B_2O_7$ materials [17] and ∼40 meV/f.u. in Aurivillius $SrBi_2(Nb,Ta)_2O_9$ [44]. Compared with these other families of layered perovskites, the $Li_2AB_2O_7$ materials have exceptionally flat energy surfaces which may enhance polar/antipolar phase competition in these materials.

We also find a very low energy barrier between the *Pnam* and $A2_1am$ phases (2.30 meV/f.u. for $Li_2SrNb_2O_7$), which can facilitate an antipolar-polar transition and antiferroelectricity. Based on this low energy and the compatibility of the domains of the *Pnam* and $A2_1am$ structures, we expect the presence of stacking domain walls in bulk *Pnam*-phase samples, where domains with antipolar distortions in opposite directions are stacked along [001]. The local structure at the stacking domain wall has $A2_1am$ symmetry, and we propose that the motion of these walls will facilitate an antipolar-polar transition. We suggest atomic-scale imaging to explore these stacking domain walls in $Li_2SrNb_2O_7$ and other Li-based materials. Stacking domain walls play an important role in the ferroelectric switching process in hybrid improper ferroelectrics such as $Ca_3Ti_2O_7$ [17] and $Sr_3Sn_2O_7$ [13,14].

Finally, we show that epitaxial strain tunes the relative energy of the *Pnam* and $A2_1am$ phases. Whereas $Li_2SrNb_2O_7$ and $Li_2CaTa_2O_7$ remain in a *Pnam* ground state for all strains we consider, we find that $A2_1am$ becomes the ground state of $Li_2CaNb_2O_7$ beyond ∼1.5% tensile strain. Thus, strain appears to be a promising knob to tune the competing *Pnam* and $A2_1am$ phases. Taken together, our results provide understanding of the competing antipolar and polar phases in the $Li_2AB_2O_7$ materials and suggest mechanisms for tuning between these phases. We hope that this motivates future exploration of these complex materials for deployment as lead-free antiferroelectrics.

The data that support the findings of this paper are provided in a Dryad repository [45].

ACKNOWLEDGMENTS

This paper was supported by the Office of Naval Research under Contract No. N00014-21-1-2957. This paper used the Expanse cluster at the San Diego Supercomputing Center through allocation PHY200085 from the Advanced Cyberinfrastructure Coordination Ecosystem: Services and Support program, which is supported by National Science Foundation Grants No. 2138259, No. 2138286, No. 2138307, No. 2137603, and No. 2138296. We also acknowledge the use of computing time at the Multi-Environment Computer for Exploration and Discovery (MERCED) and Pinnacles clusters at University of California, Merced, which are funded by National Science Foundation Grants No. ACI-1429783 and No. MRI-2019144, respectively.

APPENDIX A: STRUCTURAL PROPERTIES

This Appendix provides additional information on the structural phases of the $Li_2AB_2O_7$ materials analyzed in Secs. III–IV of the main text. Table IV reports the lattice parameters of all structural phases given in Table II. When available, the experimental lattice parameters are reported for comparison. Table V reports the structural distortion amplitudes.

APPENDIX B: ENERGY SURFACES

Energy surfaces computed for $Li_2SrTa_2O_7$, $Li_2CaNb_2O_7$, and $Li_2CaTa_2O_7$ are given in Figs. 7–9. Landau coefficients

TABLE VIII. Coefficients obtained by fitting the energy surfaces of $Li_2CaTa_2O_7$ in Fig. 9 to the Landau expansions given in Eqs. (1) and (2).

	Sub-indices					
Coefficients (units)	1	2	3	4	5	6
α (meV/Å^{2}f.u.)	−162.47	−104.46	−10.92	−39.46	–	–
β (meV/Å^{4}f.u.)	28.84	39.55	187.66	213.78	–	–
γ (meV/Å^{3}f.u.)	−277.85	−204.66	–	–	–	–
δ (meV/Å^{4}f.u.)	49.83	53.94	66.74	49.83	55.39	64.79

TABLE IX. Comparison of atomic displacements contributing to the M_5^- and Γ_5^- distortions in $Li_2CaNb_2O_7$ and $Li_2CaTa_2O_7$ obtained by different methods. For the M_5^- distortion, the displacements listed in the *Pnam* column are obtained from decomposition of the DFT-relaxed *Pnam* structure, whereas those in the *Amam* column are obtained from decomposition of the DFT-relaxed $Amam(M_5^-)$ structure. For the Γ_5^- distortion, the displacements listed in the $A2_1am$ column are obtained from decomposition of the DFT-relaxed $A2_1am$ structure, whereas those in the $F2mm$ column are obtained from decomposition of the DFT-relaxed $F2mm$ structure. All displacements are given in Å for a 48-atom cell.

	$Li_2CaNb_2O_7$				$Li_2CaTa_2O_7$			
	M_5^-		Γ_5^-		M_5^-		Γ_5^-	
Atom	*Pnam*	*Amam*	$A2_1am$	$F2mm$	*Pnam*	*Amam*	$A2_1am$	$F2mm$
Li	0.10	0.09	0.03	0.08	0.03	0.03	0.01	0.04
Ca	0.64	0.64	−0.54	−0.53	0.52	0.42	−0.48	−0.38
Nb/Ta	−0.39	−0.43	−0.26	−0.27	−0.13	−0.16	−0.09	−0.09
O1	0.23	0.14	0.33	0.25	0.24	0.12	0.28	0.16
$O2_{\parallel}$	0.06	0.10	0.08	0.06	0.00	0.04	0.05	0.03
$O2_{\perp}$	0.10	0.05	0.22	0.20	0.17	0.05	0.21	0.12
O3	−0.11	−0.01	0.08	0.13	−0.12	−0.01	−0.03	0.05
Total	0.80	0.79	0.73	0.69	0.63	0.47	0.60	0.44

obtained by fitting these energy surfaces to Eqs. (1) and (2) are given in Tables VI–VIII.

A subtlety that arises in the computation of these energy surfaces is the decision about which atomic displacement patterns to use when constructing a distortion to freeze in. For example, structural relaxation of the *Pnam* structure yields a particular set of atomic displacements that transform like M_5^-, whereas structural relaxation of $Amam(M_5^-)$ yields a slightly different set of displacements. A similar issue arises when considering the displacements that transform like Γ_5^- when they are derived from the the $A2_1am$- vs the $F2mm$-relaxed structures. These differences are very slight for $Li_2SrNb_2O_7$; however, they are more significant for the Ca-based materials. Table IX compares these two sets of atomic displacements for $Li_2CaNb_2O_7$ and $Li_2CaTa_2O_7$. Inspection of Table IX reveals small differences in relative displacement contributions: For example, for $Li_2CaTa_2O_7$, the relative size of the Ca compared with the O1 displacement is $0.42/0.12 = 3.5$ with the $Amam(M_5^-)$-derived displacements, whereas it is $0.52/0.24 = 2.2$ with the *Pnam*-derived displacements. Although these differences are subtle, energy surfaces computed with these different sets of displacement patterns reveal some differences, as shown in Fig. 10. When using the *Pnam*- and $A2_1am$-derived displacements, the Γ_5^- energy surface has a slightly lower minimum energy than the M_5^- energy surface (solid lines). However, using the $Amam(M_5^-)$- and $F2mm$-derived displacements shows the opposite (dotted lines): The M_5^- energy surface has a lower energy minimum than the Γ_5^- surface. These choices affect the values of the Landau coefficients obtained from fitting, which is illustrated in Table X. Although we notice some differences in the coefficient values (particularly for the α coefficients for $LiCa_2Ta_2O_7$), we note that the energy scale of the resulting Γ_5^- and M_5^- energy surfaces (10–30 meV/f.u.) is an order of magnitude lower than the energy scale of the trilinear coupling terms (200 meV/f.u. or more). Thus, the choice we make for the $\alpha_{3,4}$ and $\beta_{3,4}$ coefficients does not affect the overall scenario.

We note that, for consistency, all energy surface plots in this paper (except for the surfaces shown with dashed lines in Fig. 10) employ distortions constructed from atomic displacements obtained from decomposing the DFT-relaxed *Pnam* and $A2_1am$ structures. All Landau coefficients are obtained by fitting energy surfaces using the *Pnam*- and $A2_1am$-derived atomic displacements for all distortions.

TABLE X. Coefficients obtained by fitting the energy surfaces of $Li_2CaNb_2O_7$ and $Li_2CaTa_2O_7$ in Fig. 10 utilizing the distortion amplitude contribution from $A2_1am$ and $Fmm2$; and *Pnam* and *Amam*.

		Subindices			
		3		4	
Materials	Coefficients (units)	*Pnam*	*Amam*	$A2_1am$	$Fmm2$
$Li_2CaNb_2O_7$	α (meV/Å^{2}f.u.)	−136.65	−148.88	−189.46	−18.22
	β (meV/Å^{4}f.u.)	181.70	158.70	289.03	251.02
$Li_2CaTa_2O_7$	α (meV/Å^{2}f.u.)	−10.92	−58.10	−39.46	−64.42
	β (meV/Å^{4}f.u.)	187.66	162.96	213.78	212.45

[1] J. Scott, Science **315**, 954 (2007).

[2] K. M. Rabe, C. H. Ahn, and J.-M. Triscone, *Physics of Ferroelectrics: A Modern Perspective*, Vol. 105 (Springer-Verlag, Berlin, 2007).

[3] K. M. Rabe, in *Functional Metal Oxides*, edited by S. B. Ogale, T. V. Benkatesan, and M. G. Blamire (Wiley, Hoboken, 2013).

[4] J. K. Burdett, Inorg. Chem. **20**, 1959 (1981).

[5] R. E. Cohen, Nature (London) **358**, 136 (1992).

[6] A. Tagantsev, K. Vaideeswaran, S. Vakhrushev, A. Filimonov, R. Burkovsky, A. Shaganov, D. Andronikova, A. Rudskoy, A. Baron, H. Uchiyama *et al.*, Nat. Commun. **4**, 2229 (2013).

[7] J. Íñiguez, M. Stengel, S. Prosandeev, and L. Bellaiche, Phys. Rev. B **90**, 220103(R) (2014).

[8] N. A. Benedek and C. J. Fennie, Phys. Rev. Lett. **106**, 107204 (2011).

[9] N. A. Benedek, J. M. Rondinelli, H. Djani, P. Ghosez, and P. Lightfoot, Dalton Trans. **44**, 10543 (2015).

[10] Y. S. Oh, X. Luo, F.-T. Huang, Y. Wang, and S.-W. Cheong, Nat. Mater. **14**, 407 (2015).

[11] S. Yoshida, K. Fujita, H. Akamatsu, O. Hernandez, A. Sen Gupta, F. G. Brown, H. Padmanabhan, A. S. Gibbs, T. Kuge, R. Tsuji *et al.*, Adv. Funct. Mater. **28**, 1801856 (2018).

[12] S. Yoshida, H. Akamatsu, R. Tsuji, O. Hernandez, H. Padmanabhan, A. Sen Gupta, A. S. Gibbs, K. Mibu, S. Murai, J. M. Rondinelli *et al.*, J. Am. Chem. Soc. **140**, 15690 (2018).

[13] Y. Wang, F.-T. Huang, X. Luo, B. Gao, and S.-W. Cheong, Adv. Mater. **29**, 1601288 (2017).

[14] X. Xu, Y. Wang, F.-T. Huang, K. Du, E. A. Nowadnick, and S.-W. Cheong, Adv. Funct. Mater. **30**, 2003623 (2020).

[15] X.-Z. Lu and J. M. Rondinelli, Nat. Mater. **15**, 951 (2016).

[16] X.-Z. Lu and J. M. Rondinelli, Adv. Funct. Mater. **27**, 1604312 (2017).

[17] E. A. Nowadnick and C. J. Fennie, Phys. Rev. B **94**, 104105 (2016).

[18] F.-T. Huang, F. Xue, B. Gao, L. Wang, X. Luo, W. Cai, X.-Z. Lu, J. Rondinelli, L. Chen, and S.-W. Cheong, Nat. Commun. **7**, 1 (2016).

[19] L. Miao, K. Hasin, P. Moradifar, D. Mukherjee, K. Wang, S.-W. Cheong, E. A. Nowadnick, and N. Alem, Nat. Commun. **13**, 4927 (2022).

[20] N. Floros, C. Michel, M. Hervieu, and B. Raveau, J. Mater. Chem. **9**, 3101 (1999).

[21] P. Ramakrishnan, H. Kwak, Y.-H. Cho, and J. H. Kim, ChemElectroChem **5**, 1265 (2018).

[22] C. Galven, J.-L. Fourquet, E. Suard, M.-P. Crosnier-Lopez, and F. Le Berre, Dalton Trans. **39**, 4191 (2010).

[23] R. Uppuluri, H. Akamatsu, A. Sen Gupta, H. Wang, C. M. Brown, K. E. Agueda Lopez, N. Alem, V. Gopalan, and T. E. Mallouk, Chem. Mater. **31**, 4418 (2019).

[24] T. Nagai, H. Shirakuni, A. Nakano, H. Sawa, H. Moriwake, I. Terasaki, and H. Taniguchi, Chem. Mater. **31**, 6257 (2019).

[25] A. Nakano, H. Shirakuni, T. Nagai, Y. Mochizuki, F. Oba, H. Yokota, S. Kawaguchi, I. Terasaki, and H. Taniguchi, Phys. Rev. Mater. **6**, 044412 (2022).

[26] C. Galven, D. Mounier, B. Bouchevreau, E. Suard, A. Bulou, M.-P. Crosnier-Lopez, and F. L. Berre, Inorg. Chem. **55**, 2309 (2016).

[27] Y. Mochizuki, T. Nagai, H. Shirakuni, A. Nakano, F. Oba, I. Terasaki, and H. Taniguchi, Chem. Mater. **33**, 1257 (2021).

[28] X. Xu, F.-T. Huang, K. Du, and S.-W. Cheong, Adv. Mater. **34**, 2206022 (2022).

[29] T. Pagnier, N. Rosman, C. Galven, E. Suard, J. Fourquet, F. Le Berre, and M.-P. Crosnier-Lopez, J. Solid State Chem. **182**, 317 (2009).

[30] T. Nagai, Y. Mochizuki, H. Shirakuni, A. Nakano, F. Oba, I. Terasaki, and H. Taniguchi, Chem. Mater. **32**, 744 (2020).

[31] H. Iwasaki and T. Ikeda, J. Phys. Soc. Jpn. **18**, 157 (1963).

[32] U. T. Höchli, H. E. Weibel, and L. A. Boatner, Phys. Rev. Lett. **39**, 1158 (1977).

[33] B. Zhang, Z. Hu, B. Chen, X. Liu, and X. Chen, J. Mater. **6**, 593 (2020).

[34] V. A. Cascos, J. Roberts-Watts, C. Skingle, I. Levin, W. Zhang, P. S. Halasyamani, M. C. Stennett, N. C. Hyatt, E. Bousquet, and E. E. McCabe, Chem. Mater. **32**, 8700 (2020).

[35] G. Kresse and J. Hafner, J. Phys.: Condens. Matter **6**, 8245 (1994).

[36] G. Kresse and D. Joubert, Phys. Rev. B **59**, 1758 (1999).

[37] J. P. Perdew, A. Ruzsinszky, G. I. Csonka, O. A. Vydrov, G. E. Scuseria, L. A. Constantin, X. Zhou, and K. Burke, Phys. Rev. Lett. **100**, 136406 (2008).

[38] G. Kresse and J. Furthmüller, Comput. Mater. Sci. **6**, 15 (1996).

[39] G. Henkelman, B. P. Uberuaga, and H. Jónsson, J. Chem. Phys. **113**, 9901 (2000).

[40] H. T. Stokes, D. M. Hatch, B. J. Campbell, and D. E. Tanner, J. Appl. Crystallogr. **39**, 607 (2006).

[41] K. Momma and F. Izumi, J. Appl. Crystallogr. **41**, 653 (2008).

[42] J. Perez-Mato, M. Aroyo, A. García, P. Blaha, K. Schwarz, J. Schweifer, and K. Parlinski, Phys. Rev. B **70**, 214111 (2004).

[43] U. Petralanda and I. Etxebarria, Phys. Rev. B **91**, 184106 (2015).

[44] N. Pokhrel and E. A. Nowadnick, Phys. Rev. B **107**, 054108 (2023).

[45] K.-E. Hasin and E. A. Nowadnick, Dryad Dataset (2023), doi:10.5061/dryad.ghx3ffbvf.